Diffuse-Interface Simulations of Drop Coalescence and Retraction in Complex Fluids

Pengtao Yue[1], James J. Feng[1], Chun Liu[2] and Jie Shen[3]

[1]Department of Chemical and Biological Engineering and Department of Mathematics
University of British Columbia, Vancouver, BC V6T 1Z4, Canada

[2]Department of Mathematics, The Pennsylvania State University, University Park, PA 16802, USA

[3]Department of Mathematics, Purdue University, West Lafayette, IN 47907, USA

Abstract - Drop dynamics plays a central role in defining the interfacial morphology in two-phase complex fluids such as emulsions and polymer blends. In such materials, the components are often microstructured complex fluids themselves. To model and simulate drop behavior in such systems, one has to deal with the dual complexity of non-Newtonian rheology and evolving interfaces. Recently, we developed a diffuse-interface formulation which incorporates complex rheology and interfacial dynamics in a unified framework. This paper describes applications of our method to simulate drop coalescence after head-on collision and drop retraction in a quiescent matrix. One of the two phases is Newtonian and the other is rheologically complex; we have considered viscoelastic fluids modeled by an Oldroyd-B equation and nematic liquid crystals described by a modified Leslie-Ericksen model. After two drops collide, film drainage is enhanced when either phase is viscoelastic and drop coalescence happens more readily than in a comparable Newtonian system. The retraction of drops from a stationary state of zero-velocity and zero-stress is initially hastened but eventually hindered by viscoelasticity in either component. Newtonian theories may be used to back out the interfacial tension only if the polymer relaxation time is much shorter than the drop retraction time. When retracting from an initial state with pre-existing stress, as produced by steady shearing, viscoelasticity in the matrix hinders retraction from the beginning while that in the drop initially enhances retraction but later resists it. The retraction of nematic drops reveals interactions among surface tension, surface anchoring and bulk orientation. The dynamic interfacial tension drives a Marangoni flow near the isotropic-nematic interface. In general, the retraction process cannot be used as a means of measuring the interfacial tension between a liquid crystalline polymer and a flexible polymer.

I. INTRODUCTION

Drop dynamics is the key to understanding interfacial morphology in two-phase materials. In nature and in industrial processes, many such materials have components that are complex fluids themselves, with internal microstructures whose evolution affects the macroscopic dynamics of the material, especially the rheology. Examples include polymer blends [Utracki (1990)], polymer-dispersed liquid crystals [West (1990)] and various biological fluids [e.g., Dintenfass (1990)].

Theoretical and numerical analysis of drop dynamics in complex fluids has to struggle with the dual difficulties of moving interfaces and microstructure-dependent rheology. Specifically, there is the interplay among microscopic, mesoscopic and macroscopic scales: (a) the internal microstructure, e.g., molecular conformation, inside each component, (b) the interfaces, and (c) the flow field. The coupling between (b) and (c) alone is well studied for Newtonian drops [Stone (1994)]. Similarly, the (a)-(c) coupling is the subject of molecular constitutive theories in rheology [e.g., Feng *et al.* (2000)]. Having both (a) and (b) present in a flow problem, and indeed *coupled* as in the nematic drop retraction to be discussed in Section IV, is the novelty of this work.

Methods for solving moving-interface problems fall into two broad categories: interface tracking and interface capturing [Sethian and Smereka (2003); Tezduyar (2003)]. The former uses a moving mesh with grid points residing on the interface. The latter determines the position of the interface by using a scalar function, whose evolution is typically represented by an advection equation on a fixed grid. Conceptually, the interface is seen as a zero-thickness surface in either case, though an essential ingredient in the fixed-grid methods is a numerical regularization that spreads the interfacial force over a volume.

Recently, Yue *et al.* (2004) proposed a fixed-grid *diffuse-interface model* for two-phase flows of complex fluids. This model differs from other fixed-grid methods in that the interface is treated as *physically* diffuse. The interfacial position and thickness are determined by a phase-field variable whose evolution is governed by a mixing energy. This way, the structure of the interface is rooted in molecular forces; the tendencies for mixing and demixing are balanced through the nonlocal mixing energy. In contrast, the level set and volume-of-fluid methods replace the surface tension by a body force or stress as a *numerical* device to

regularize the singularity. When the interfacial width approaches zero, the diffuse-interface model becomes identical to a sharp-interface level-set formulation. It also reduces properly to the classical sharp-interface model.

The diffuse-interface method has been applied to numerous interfacial problems [e.g., Anderson *et al.* (1998); Liu and Shen (2003)]. In our context of two-phase complex fluids, its main attraction is the capability of easily incorporating the rheology of microstructured fluids. This is by virtue of its energy-based variational formalism. As long as the conformation of the microstructure is describable by a free energy, this energy can be added to the mixing energy to form the total free energy of the multi-phase system. Then a formal variational procedure applied to the total free energy will give rise to the proper constitutive equation for the microstructured fluids in addition to the evolution equation of the phase field variable. Using the Frank distortion energy for a liquid crystal and the Hookean-dumbbell energy for a polymer chain, Yue *et al.* (2004) illustrated how interfacial dynamics and complex rheology can be included in a *unified* theoretical framework. Dissipative effects such as viscous stresses, of course, have to be accounted for separately, e.g., via the standard irreversible thermodynamic procedure [Lowengrub and Truskinovsky (1998)] or by including Brownian motion in Hamilton's principle [Peskin (1985); Gliklikh (1997)].

Yue *et al.* (2004) have implemented the diffuse-interface method using a spectral representation, and presented preliminary numerical results to validate the theoretical model and the numerical method. The goal of this paper is to apply the method to physically interesting problems where it generates new insights into the physics. We will investigate two flow problems: drop coalescence after head-on collision and drop retraction.

II. THEORY AND NUMERICAL METHOD

A detailed derivation of the model and a description of the numerical scheme have been given by Yue *et al.* (2004). We will summarize the salient features here.

The formulation applies to any microstructured fluid describable by a free energy. As an example, let us consider the immiscible blend of a Newtonian liquid and a nematic liquid crystal. There are three types of free energies in this system: mixing energy of the interface, bulk distortion energy of the nematic, and the anchoring energy of the liquid crystal molecules on the interface.

The diffuse-interface has a small but non-zero thickness, inside which the two components are mixed and store a mixing energy. We define a phase-field variable ϕ such that the concentrations of the nematic and Newtonian components are $(1+\phi)/2$ and $(1-\phi)/2$, respectively. For the mixing energy, we adopt the familiar Ginzburg-Landau form:

$$f_{mix}(\phi, \nabla\phi) = \frac{1}{2}\lambda|\nabla\phi|^2 + \frac{\lambda}{4\epsilon^2}(\phi^2-1)^2, \tag{1}$$

where λ is the mixing energy density (with the dimension of force), and ϵ is a capillary width that scales with the thickness of the diffuse interface. As $\epsilon \to 0$, the ratio λ/ϵ produces the interfacial tension in the classical sense [Jacqmin (1999); Yue *et al.* (2004)]. The bulk of the nematic phase has a Frank distortion energy, which we write as [de Gennes and Prost (1993); Lin and Liu (1995)]:

$$f_{bulk} = K\left[\frac{1}{2}\nabla\boldsymbol{n} : (\nabla\boldsymbol{n})^{\mathrm{T}} + \frac{(|\boldsymbol{n}|^2-1)^2}{4\delta^2}\right], \tag{2}$$

where $\boldsymbol{n}$ is the director and K is the elastic constant in the one-constant approximation. The second term on the right hand side regularizes the classical Frank energy to permit defects where $|\boldsymbol{n}|$ deviates from unity over a small region of size δ [Liu and Walkington (2000)]. Finally, we adapt the Rapini-Popoular form of the anchoring energy, which, in our diffuse-interface picture, is written as a volumetric energy density:

$$f_{anch} = \tfrac{A}{2}(\boldsymbol{n}\cdot\nabla\phi)^2 \quad \text{for planar anchoring,} \tag{3}$$

$$f_{anch} = \tfrac{A}{2}[|\boldsymbol{n}|^2|\nabla\phi|^2 - (\boldsymbol{n}\cdot\nabla\phi)^2] \quad \text{for homeotropic anchoring,} \tag{4}$$

where A is the anchoring energy density. Now we have the total free energy density for the two-phase material:

$$f(\phi, \boldsymbol{n}, \nabla\phi, \nabla\boldsymbol{n}) = f_{mix} + \frac{1+\phi}{2}f_{bulk} + f_{anch}. \tag{5}$$

Note that $\phi = 1$ and -1 in the bulk nematic and Newtonian phases, respectively.

Following a variational procedure detailed in Yue *et al.* (2004), evolution equations for all the configuration variables ($\boldsymbol{v}$, ϕ and $\boldsymbol{n}$ in this case) can be derived. After being supplemented by the appropriate dissipative terms, these are essentially the governing equations familiar in the classical context. For $\boldsymbol{v}$, we have

$$\nabla\cdot\boldsymbol{v} = 0, \tag{6}$$

$$\rho\left(\frac{\partial \boldsymbol{v}}{\partial t}+\boldsymbol{v}\cdot\nabla\boldsymbol{v}\right)=-\nabla p+\nabla\cdot\boldsymbol{\sigma}, \tag{7}$$

where the deviatoric stress tensor $\boldsymbol{\sigma}$ has an elastic and a viscous component. The former can be derived from a virtual work principle [Yue *et al.* (2004)]:

$$\boldsymbol{\sigma}^e=-\lambda(\nabla\phi\otimes\nabla\phi)-K\frac{1+\phi}{2}(\nabla\boldsymbol{n})\cdot(\nabla\boldsymbol{n})^{\mathrm{T}}-\boldsymbol{G}, \tag{8}$$

where $\boldsymbol{G}=A(\boldsymbol{n}\cdot\nabla\phi)\boldsymbol{n}\otimes\nabla\phi$ for planar anchoring and $\boldsymbol{G}=A[(\boldsymbol{n}\cdot\boldsymbol{n})\nabla\phi-(\boldsymbol{n}\cdot\nabla\phi)\boldsymbol{n}]\otimes\nabla\phi$ for homeotropic anchoring. Note that the anchoring energy f_{anch}, through $\boldsymbol{G}$, induces a Marangoni force along isotropic-nematic interfaces [Rey (2000)]. In addition, a Newtonian viscous stress is assumed:

$$\boldsymbol{\sigma}^v=\mu[\nabla\boldsymbol{v}+(\nabla\boldsymbol{v}^T)], \tag{9}$$

where the viscosity μ may generally be different in the two phases. The relaxation of ϕ is governed by the celebrated Cahn-Hilliard equation [Cahn and Hilliard (1959)]:

$$\frac{\partial\phi}{\partial t}+\boldsymbol{v}\cdot\nabla\phi=\gamma_1\lambda\nabla^2\left[-\nabla^2\phi+\frac{\phi(\phi^2-1)}{\epsilon^2}\right], \tag{10}$$

where γ_1 is the mobility constant. As we are concerned with very thin interfaces between nominally immiscible fluids, it is impractical to use interfacial relaxation as a criterion for choosing γ_1. Rather it is determined based on maintaining a more or less uniform interface without overly damping the flow [Jacqmin (1999); Yue *et al.* (2004)]. Finally, the evolution equation of $\boldsymbol{n}$ is written as:

$$\frac{\partial\boldsymbol{n}}{\partial t}+\boldsymbol{v}\cdot\nabla\boldsymbol{n}=\gamma_2\boldsymbol{h}, \tag{11}$$

where the molecular field $\boldsymbol{h}$ arises from the free energies of the system [de Gennes and Prost (1993)]:

$$\boldsymbol{h}=-\frac{\delta F}{\delta\boldsymbol{n}}=K\left[-\nabla\cdot\left(\frac{1+\phi}{2}\nabla\boldsymbol{n}\right)+\frac{1+\phi}{2}\frac{(\boldsymbol{n}^2-1)\boldsymbol{n}}{\delta^2}\right]+\boldsymbol{g}, \tag{12}$$

with $\boldsymbol{g}=A(\boldsymbol{n}\cdot\nabla\phi)\nabla\phi$ for planar anchoring, and $\boldsymbol{g}=A[(\nabla\phi\cdot\nabla\phi)\boldsymbol{n}-(\boldsymbol{n}\cdot\nabla\phi)\nabla\phi]$ for homeotropic anchoring. The constant γ_2 determines the relaxation time of the director field.

One notes that equations (8), (9) and (11) constitute a "stripped-down" version of the Leslie-Ericksen theory [de Gennes and Prost (1993)], with the viscous torque due to straining flow omitted from Eq. (11) and the anisotropic viscous terms from Eq. (9). The

rationale for leaving out these dissipative terms is two-fold. First, the conservative dynamics dictates the trend in the system's evolution, while dissipation plays the secondary role of slowing down the process. Second, neglecting these terms brings about considerable savings in computation. If retained, they would couple the momentum equation closely with the director evolution, and entail iteration among the equations at every time step. By omitting these terms, we can solve the system semi-implicitly without iterations. Restoring them constitutes numerical complications but no conceptual difficulty [Lin and Liu (2000)]. For numerical convenience, we have only computed equal-viscosity cases in this paper.

Yue *et al.* (2004) developed a two-dimensional spectral method for these governing equations, and an interested reader can find details of the numerical algorithm there. To enhance stability, we advance time semi-implicitly, with the nonlinear transport terms treated explicitly while the linear terms implicitly. Depending on the periodicity of the boundary condition in each direction, a Fourier or Chebyshev-Galerkin method is used to discretize the spatial derivatives on a regular grid. The treatment of non-periodic boundary conditions entails splitting the Cahn-Hilliard equation into two Helmholtz equations to which Neumann boundary conditions apply as in Shen (1995). The number of operations per time step scales as $O(N \log N)$, N being the number of unknowns. We have carried out grid and time-step refinements to determine the adequacy of our spatial and temporal resolutions. The interface typically requires 7–10 grids to resolve, and the total number of grid points is typically 2048×1024. For the time step, we find the Courant-Friedricks-Lewy condition a useful guideline. In all cases tested, the temporal resolution is adequate as long as the simulation is stable.

III. DROP COALESCENCE AFTER HEAD-ON COLLISION

An advantage of the diffuse-interface method is its ability to handle topological changes in the interfacial morphology, and this section exploits this ability to probe the coalescence of two drops after a head-on collision. Yue *et al.* (2004) illustrated this ability by a single example of Newtonian drops coalescing in a Newtonian matrix. Here we explore two physically important issues: (a) the representation of short-range molecular forces in the diffuse-interface framework; (b) the effects of viscoelasticity in either component on the collision and coalescence.

We have adopted the scheme of Nobari *et al.* (1996) to simulate the head-on collision of two identical drops. Initially, two stationary drops of diameter D are separated by a center-to-center distance d. Then a body force $\boldsymbol{f}$ is applied to accelerate the drops toward each other. When the drop velocity attains a prescribed value $U/2$, $\boldsymbol{f}$ is turned off. The two drops collide into each other by inertia and coalesce.

A. Newtonian drops in a Newtonian matrix: molecular forces

Figure 1 illustrates a typical run for two Newtonian drops in a Newtonian matrix of the same viscosity. The initial separation between the centers of the drops is $d = 1.5D$, and the

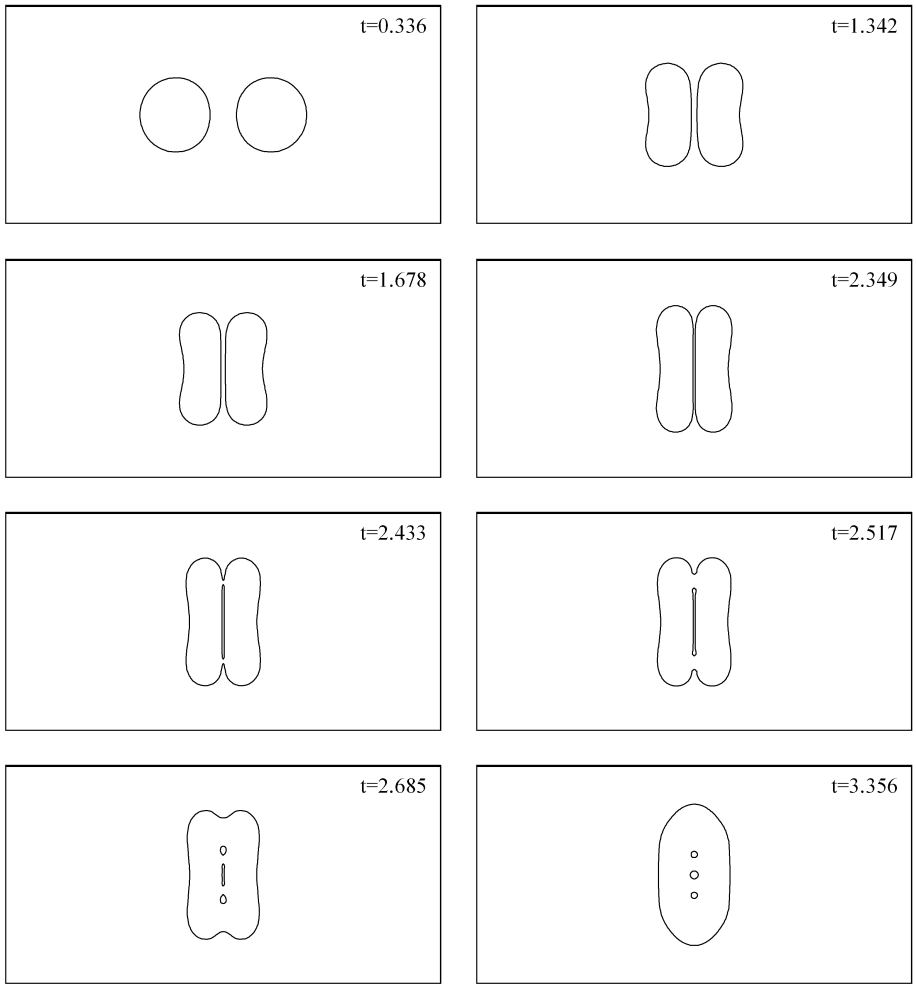

Figure 1: Collision and coalescence of two Newtonian drops in a Newtonian matrix. The Reynolds number, defined using D and U, is $Re = 33.6$, and the Weber number is $We = 12$. Other parameters are: $\epsilon = 0.01$ and $\gamma_1 = 3.365 \times 10^{-5}$ [after Yue *et al.* (2004), ©Cambridge University Press.]

body force is turned on at $t = 0$ and off at $t = 0.336$ to achieve a U value that corresponds to $Re = 33.6$. Time is scaled here by D/U. The drops deform while approaching each other ($t = 1.342$). As a result, a thin film of the matrix fluid forms between the two drops. The thinning of this film, via the drainage of the matrix fluid through the narrowing conduit, determines the time scale of coalescence. The drainage requires a high pressure in the middle of the film, which produces a "dimpled shape" for the interface [Chuang and Flumerfelt (1997)], with the minimum film thickness not at the middle point but farther out toward the sides. Rupture of the film at those locations traps a filament of the the matrix fluid inside the resultant large drop. The subsequent breakup of the filament into drops is not due to capillary instability; rather it is caused by the stretching flow due to the bulging interface [Yue *et al.* (2004)]. The most important feature, however, is that coalescence occurs "naturally" as a result of the Cahn-Hilliard dynamics (cf. Eq. 10). This contrasts sharp-interface simulations where the film separating the two drops has to be artificially removed to bring about the topological change [Nobari *et al.* (1996)].

A natural question is whether the breakage and reconnection of the interfaces simulated here reflects reality. According to our current understanding, the rupture of an interface is not a purely hydrodynamic process. As the film gets to a critical thickness of tens of nanometers, van der Waals attraction overcomes electric double-layer repulsion and causes the film to rupture and the two interfaces to merge [Bradley and Stow (1978); Bhakta and Ruckenstein (1997); Nemer *et al.* (2004)]. This type of molecular interaction is what the Cahn-Hilliard mixing energy strives to represent. In this sense, the diffuse-interface model contains the physics of short-range molecular forces. However, the form of the Cahn-Hilliard force turns out to be different from the familiar van der Waals force.

Consider a liquid film (F) of uniform thickness h sandwiched between semi-infinite domains of another fluid (A) (Fig. 2). The van der Waals interaction energy per unit area between the parallel interface can be written as [Israelachvili (1992)]:

$$E_A = -\frac{A_h}{12\pi h^2}, \tag{13}$$

where A_h is the Hamaker constant. The intervening film would in general hamper the van der Waals interaction, but we neglect this effect here for simplicity. From this energy we can get the disjoining pressure

$$\Pi \equiv p_A - p_F = -\frac{dE_A}{dh} = -\frac{A_h}{6\pi h^3}. \tag{14}$$

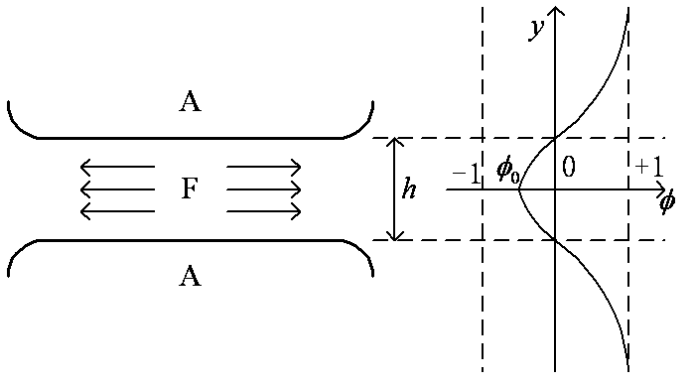

Figure 2: A draining film and the corresponding ϕ profile.

To derive the counterpart of the disjoining pressure in the diffuse-interface representation, we consider the equilibrium $\phi(y)$ profile in the configuration of Fig. 2. In the bulk phase A, $\phi \to 1$. If the film is much thicker than the interfaces ($h \gg \epsilon$), then $\phi(0)$ would approach -1 in the film phase. Since the film is thin, however, $\phi(0) = \phi_0 > -1$. Now the disjoining pressure can be calculated from the stress field. Note that the mixing energy of Eq. (1) produces an elastic stress tensor [Yue *et al.* (2004)]:

$$\boldsymbol{T} = -(p - f_{mix})\boldsymbol{I} - \lambda \nabla\phi \otimes \nabla\phi, \tag{15}$$

where p is the thermodynamic pressure, and $\boldsymbol{I}$ is the second-order unit tensor. In the bulk phase A, the normal stress in the y direction is simply $-p_A$. At the center of the film, $\left.\frac{d\phi}{dy}\right|_{y=0} = 0$ because of symmetry. Thus the normal stress there is $-p_F + \lambda f_0$, where $f_0 = (\phi_0^2 - 1)^2/4\epsilon^2$ is the local part of the mixing energy. A normal force balance then gives the disjoining pressure in the diffuse-interface model as

$$\Pi_\phi = -\lambda f_0 = -\frac{\lambda(\phi_0^2 - 1)^2}{4\epsilon^2}. \tag{16}$$

The disjoining pressure in Eq. (16) has the following in common with the van der Waals force in Eq. (14):

- The disjoining pressure is negative, indicating attraction between the two interfaces;
- The attraction is a short-distance force. It becomes significant only if the film is sufficiently thin ($h \sim \epsilon$); for large h, both Π and Π_ϕ vanish.

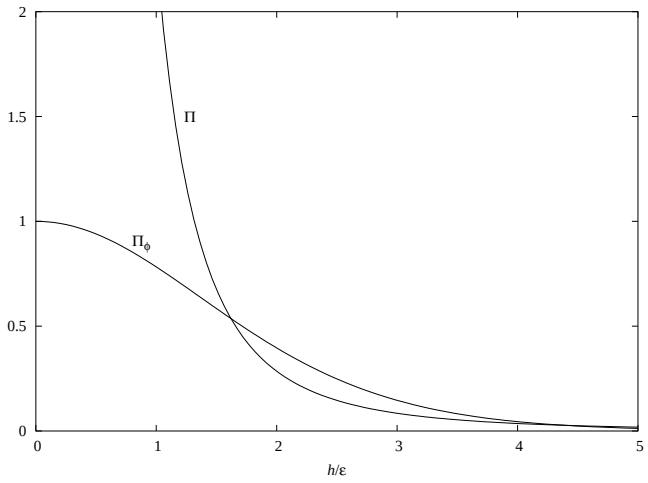

Figure 3: Comparison of the disjoining pressure Π_ϕ in the diffuse-interface model, computed from Eqs. (16) and (19), with Π of Eq. (18) derived from the van der Waals force. The two pressures are scaled by $-\lambda/4\epsilon^2$, and we have assumed $\epsilon = \xi$ in Eq. (18).

There are notable differences, however. As $h \to 0$, the van der Waals force diverges: $\Pi \to \infty$. On the other hand, as the two diffuse interfaces merge, $\phi_0 \to 0$ and Π_ϕ approaches a finite value $-\lambda/4\epsilon^2$. For a film of thickness $h \sim \epsilon$, the two expressions for the disjoining pressure have the same order of magnitude. This can be seen by noting the connection between the Hamaker constant and the surface tension [Israelachvili (1992)]:

$$\sigma = \frac{\sqrt{3}}{2\pi^2}\frac{A_h}{\xi^2}, \tag{17}$$

where ξ is the intermolecular center-to-center distance. Noting that $\sigma = \frac{2\sqrt{2}}{3}\frac{\lambda}{\epsilon}$ [see Yue *et al.* (2004)], we transform Eq. (14) into

$$\Pi = -\frac{2\sqrt{2}\pi}{9\sqrt{3}}\frac{\lambda}{\epsilon^2}\left(\frac{\xi}{\epsilon}\right)^2\left(\frac{\epsilon}{h}\right)^3, \tag{18}$$

which, for $h \sim \epsilon \sim \xi$, is on the same order as Π_ϕ in Eq. (16). To estimate Π_ϕ for a non-vanishing h, we may assume a hyperbolic tangent ϕ-profile as in a single 1D equilibrium interface [Yue *et al.* (2004)]. Then the phase-field function in the middle of the film can be estimated to be

$$\phi_0 = -\tanh\left(\frac{h}{2\sqrt{2}\epsilon}\right). \tag{19}$$

Inserting this into Eq. (16), we illustrate the quantitative differences between Π_ϕ and Π at different h values in Fig. 3. On a fundamental level, the discrepancy between Π and Π_ϕ

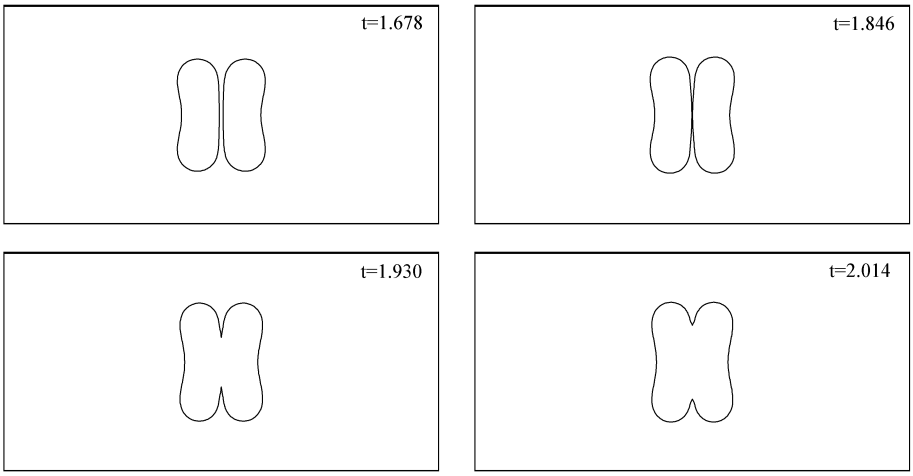

Figure 4: Collision and coalescence of two Newtonian drops in a Newtonian matrix with a thicker interface. The parameters are the same as Fig. 1 except for $\epsilon = 0.02$.

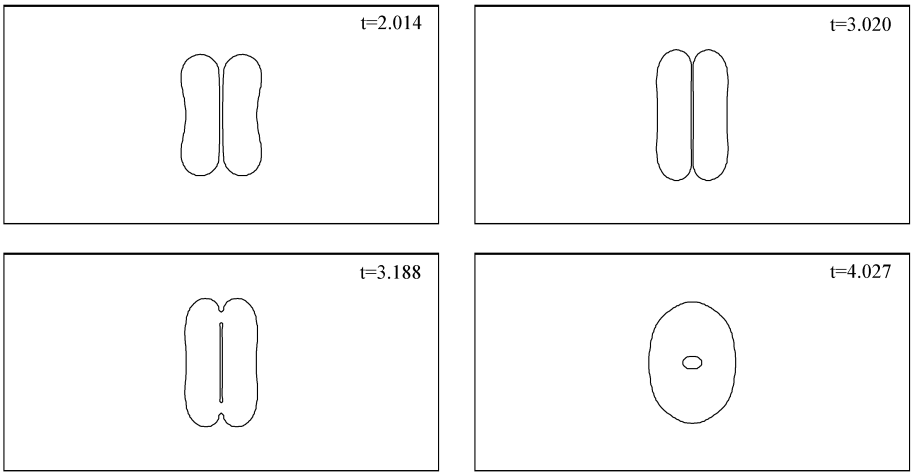

Figure 5: Collision and coalescence of two Newtonian drops in a Newtonian matrix with a thinner interface. The parameters are the same as Fig. 1 except for $\epsilon = 0.005$.

stems from the truncation of the Cahn-Hilliard free energy at the quadratic term $|\nabla\phi|^2$. An elegant explanation has been given by Pismen (2001).

Besides the disjoining pressure, two additional factors affect the film drainage and rupture in a diffuse-interface framework. The first is the capillary thickness ϵ, which can be seen as a measure of the thickness of the interface. Figures 4 and 5 show simulations with a larger or smaller ϵ than in Fig. 1 with all other parameters unchanged. The early stage

of the simulations, say for $t \leq 1.342$, is identical with Fig. 1. This is before the interfacial profiles of the two drops overlap. For a larger ϵ, the interfaces of the two drops overlap at an earlier time during their approach, and the ensuing coalescence occurs more readily (Fig. 4). Note that the interface does not have time to develop the dimpled shape, and no matrix fluid is trapped inside the drop. On the other hand, a smaller ϵ prolongs the coalescence process (Fig. 5). As compared with Fig. 1, the points of rupture are more toward the ends of the film. This produces a less pronounced waist in the resultant compound drop, and the entrapped matrix filament does not break up but retracts into a droplet. The effect of ϵ is not to be confused with numerical resolution of the interface. For each ϵ, mesh refinement has confirmed that the grid used here is adequate for resolving the interface [see also Yue *et al.* (2004)]. The optimal ϵ cannot be determined by an *a priori* criterion. Rather, it needs to reflect the range of the molecular forces at work in the particular experiment to be simulated.

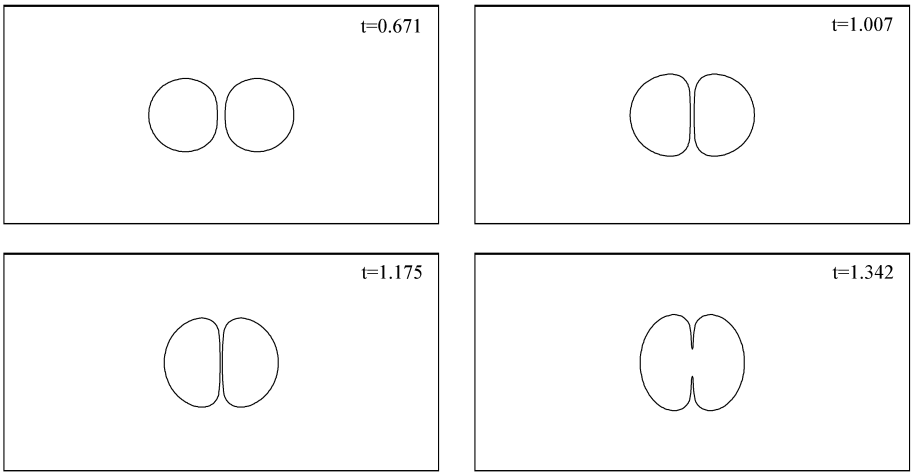

Figure 6: Collision and coalescence of two Newtonian drops in a Newtonian matrix, with initial deformation artificially suppressed by using an interfacial energy 100 times larger until $t = 0.503$. The Weber number is $We = 0.12$ before $t = 0.503$ and $We = 12$ afterwards. Other parameters are the same as Fig. 1.

The coalescence process also depends on the global curvature of the interfaces. In other words, it depends on how deformed the drops are at the start of the film drainage process. We have varied the degree of "initial deformation" by artificially using a higher surface tension (with the surface energy density λ a hundred times larger) for various lengths of

time before coalescence. An example is shown in Fig. 6 in which the higher interfacial tension, corresponding to $We = 0.12$, is applied for $t \leq 0.503$. Compared with Fig. 1, the initial deformation is smaller and the interfaces between the drops have a larger curvature. This results in a speedier film drainage and coalescence. Note also the lack of an inflection point on the interface between film rupture; no matrix fluid is entrapped in the resultant drop.

B. Role of viscoelasticity in coalescence

To investigate the role of viscoelasticity in film drainage, we compare three runs that are identical except for the rheology of the matrix or drop fluid: Newtonian drops in a Newtonian matrix (N/N), Newtonian drops in an Oldroyd-B matrix (N/O) and Oldroyd-B drops in a Newtonian matrix (O/N). The Oldroyd-B and Newtonian fluids have the same *shear* viscosity. This scheme is complicated somewhat by the fact that the coalescence process depends on the initial deformation of the drops. For two *viscoelastic* drops, the initial acceleration and approach will lead to a slightly different geometry at what may be considered the start of film drainage than for two *Newtonian* drops. To obtain a uniform initial drop shape, we place two Newtonian drops closer to each other at $d = 1.2D$ in a Newtonian matrix, accelerate them using a larger body force for a shorter period $t = 0.087$, and suppress their initial deformation by temporarily raising the interfacial energy λ by a factor of 100. At the end of the acceleration, the original λ is restored, and the phase function and velocity at $t = 0.087$ are used as the "initial condition" for all the calculations in this section including N/O and O/N cases. For the viscoelastic fluid the polymer stress is simply set to zero at $t = 0.087$. This gives us an identical "initial configuration" at $t = 0.087$ for all three runs. The N/N case is illustrated in Fig. 7. Note that the drops are essentially undeformed at $t = 0.087$, with a minimum film thickness $h_{min} = 0.171$. During film drainage, the minimum thickness always occurs at the middle of the film, and no matrix filament is trapped in the combined drop.

Figure 8 compares the thinning of the film thickness h_{min} for the three cases at several Deborah numbers. When either the matrix or the drop phase is viscoelastic, the film drainage is *faster* than for N/N. Moreover, this effect becomes stronger with increasing Deborah number De. This trend is also born out by the velocity profile of the drainage flow in various cases (Fig. 9).

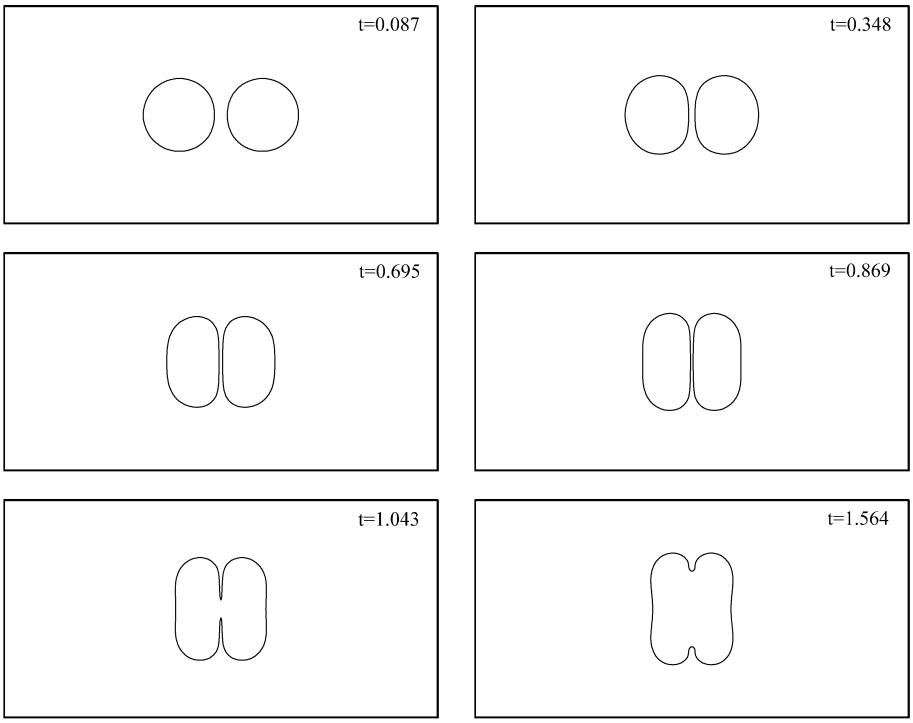

Figure 7: Collision and coalescence of two Newtonian drops in a Newtonian matrix, with initial deformation artificially suppressed by using an interfacial energy 100 times larger until $t = 0.087$. The Reynolds number is $Re = 26.1$, and the Weber number is $We = 9.6$. Other parameters are: $\epsilon = 0.01$ and $\gamma_1 = 3.48 \times 10^{-5}$.

Let us consider the N/O case first where the matrix is an Oldroyd-B fluid. The flow in the draining film is essentially planar extension; this has been verified by calculating the components of the strain-rate tensor. Figure 10 shows the temporal variation of the extensional rate $\dot{\epsilon}$ at the center of the film. While the drops accelerate toward each other, the strain rate must have increased. When the acceleration stops at $t = 0.087$ and the film drainage commences, the strain rate starts to decrease in time. The upturn toward the end is due to short-range forces discussed before, and corresponds to the precipitous decrease of film thickness just before coalescence (Fig. 8). In this final stage, the disjoining pressure $\Pi_\phi \sim \frac{\lambda}{\epsilon^2}$ [cf. Eq. (16)] is much larger than the pressure drop caused by interfacial tension $\Delta p \sim \frac{\lambda}{\epsilon D}$ and dominates the film drainage process.

The reaction of the Oldroyd-B matrix to this time-dependent squeezing flow is illustrated by the normal stress difference $N_1 = \tau_{yy} - \tau_{xx}$ and elongational viscosity $\eta = N_1/\dot{\epsilon}$ in

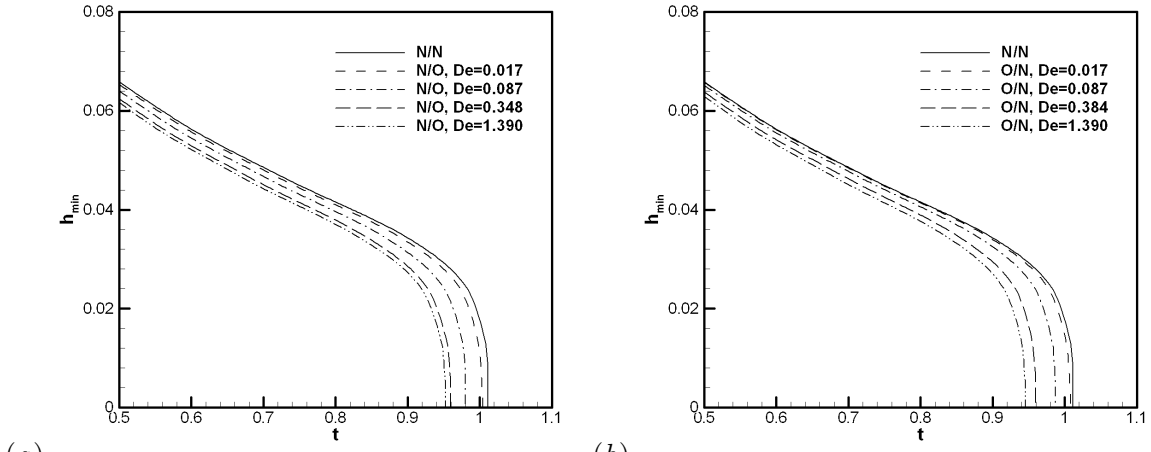

(a) (b)

Figure 8: Decrease of the minimum film thickness h_{min} during film drainage. (a) Comparison of N/O runs at 4 Deborah numbers with the N/N case; (b) comparison of O/N runs at 4 Deborah numbers with the N/N case. All other parameters are the same as in Fig. 7.

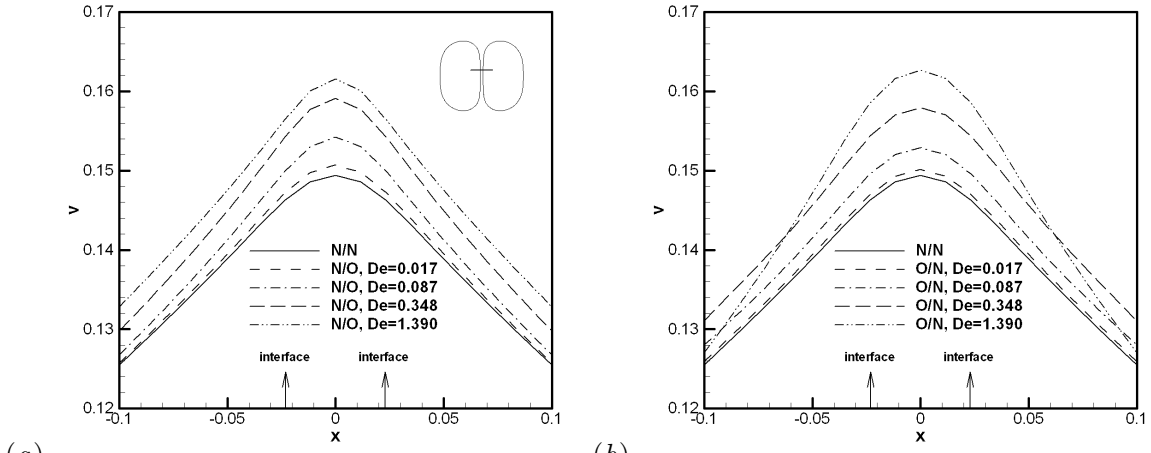

(a) (b)

Figure 9: Velocity profiles $v(x)$ along a horizontal line $y = 0.105$ (position shown in the inset) for the draining flow in Fig. 8 at $t = 0.695$. (a) Newtonian drops in an Oldroyd-B matrix (N/O); (b) Oldroyd-B drops in a Newtonian matrix (O/N). The x and y axes are along and normal to the direction of drop acceleration, with the origin at the center of the film.

Fig. 11. The Newtonian fluid has a constant η, of course, and its normal stress N_1 traces the extension rate. The Oldroyd-B fluids have lower N_1 and η at the beginning of the drainage process since the polymer chains are predominantly in the coiled state. These are stretched by the extensional flow, and continue to unravel even as $\dot{\epsilon}$ declines. Hence, a cross-over occurs both in N_1 and in η, at a time t_c that roughly scales with the polymer

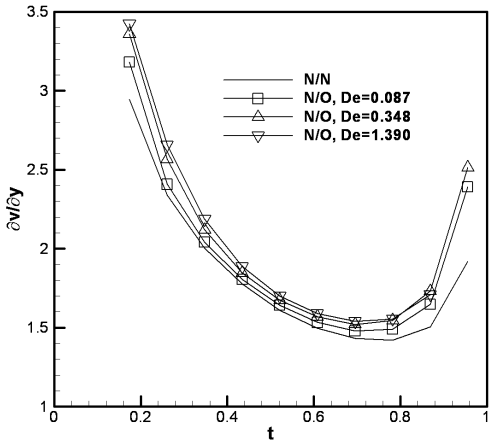

Figure 10: Variation of the extension rate $\dot{\epsilon} = \partial v/\partial y = -\partial u/\partial x$ at the center of the film during drainage. The drops are Newtonian while the matrix is Newtonian or Oldroyd-B with various relaxation times.

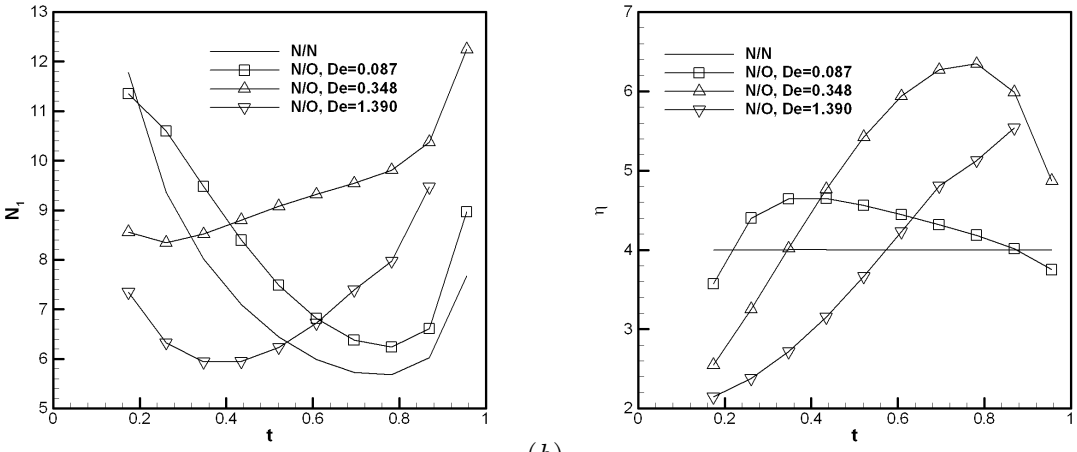

(a) (b)

Figure 11: Evolution of (a) the normal stress difference and (b) the elongational viscosity at the center of the film for the same simulations as in Fig. 10.

relaxation time. For $t < t_c$, the Oldroyd-B fluids present less elongational viscosity than the Newtonian fluid, which implies faster drainage. For $t > t_c$, on the other hand, the viscoelastic normal stress grows beyond that of the Newtonian stress. As a result, the Oldroyd-B fluids now exhibit a stronger resistance to deformation. The drainage is then hampered by viscoelasticity. This scenario is confirmed by Table 1, which lists the time Δt for the final stage of drainage from a film thickness $h_{min} = 0.04$ to 0. With increasing

test case	Δt
N/N	0.541
N/O, De=0.017	0.545
N/O, De=0.087	0.533
N/O, De=0.348	0.542
N/O, De=1.390	0.555
O/N, De=0.017	0.540
O/N, De=0.087	0.514
O/N, De=0.348	0.500
O/N, De=1.390	0.508

Table 1: Duration of the final stage of film drainage as h_{min} decreases from 0.04 to 0.

De, Δt decreases first and then increases. Δt for N/O at $De = 0.017$ being slightly longer than that of N/N is a numerical artifact due to errors in determining the exact time when h_{min} reaches 0.04. Only at large enough De can the Oldroyd-B fluid attain a stress much higher than its Newtonian counterpart, and the hardening of the polymer is felt only toward the end of the drainage process. In fact, if we measure the time taken to drain the film from a larger initial thickness $h_{min} \geq 0.06$ to 0, then the upturn for large De will not show up. To summarize, the apparent viscoelastic effect of hastening film drainage and drop coalescence in Fig. 8 is actually the integrated result of two stages of opposing tendencies. The first stage, where the polymeric matrix offers weaker resistance to extension, dominates the second stage, where the high level of viscoelastic stress suppresses film drainage.

Essentially the same argument applies to Oldroyd-B drops coalescing in a Newtonian matrix (O/N). Figure 12 illustrates the evolution of the normal stress difference N_1 and the elongational viscosity η just inside the Oldroyd-B drop (at $\phi = 0.9$). The viscous normal stress from the baseline N/N case is also shown for comparison. The viscoelastic stress is initially slow in developing but in time exceeds that of the Newtonian stress. This resembles Fig. 11 except that the viscoelastic stress now acts on the drop side of the interfaces. The effect on film drainage is the same, however, considering that the interfaces have negligible curvature over most of the film, and simply transmit the viscoelastic stress into the film. Finally, the duration of the last stage of drainage Δt first decreases with De and then turns up, in a similar way to the N/O case (Table 1).

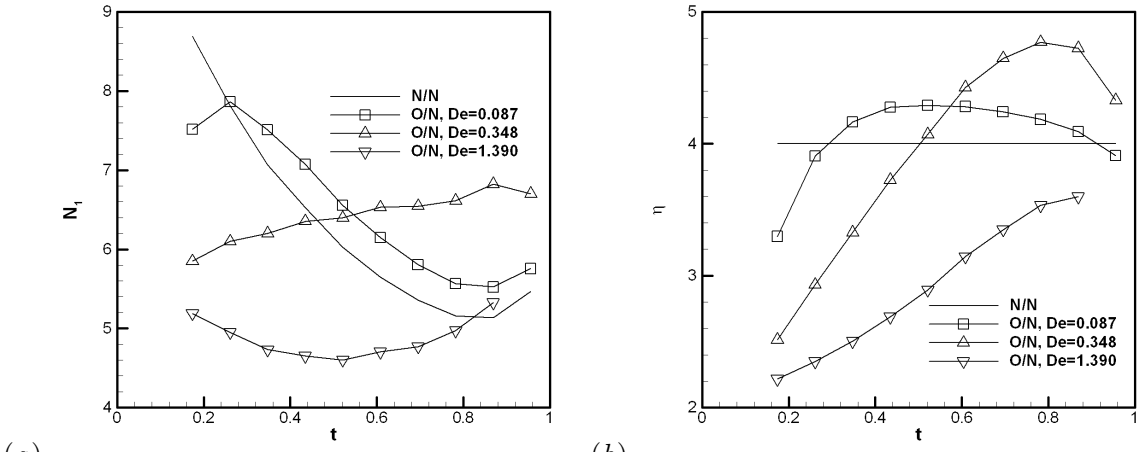

(a) (b)

Figure 12: Evolution of (a) the normal stress difference and (b) the elongational viscosity at the intersection of $y = 0$ and $\phi = 0.9$, just inside the Oldroyd-B drop. The matrix is Newtonian.

IV. DROP RETRACTION IN A QUIESCENT MEDIUM

Drop retraction is a convenient method for measuring the interfacial tension between the drop and matrix fluids [Mo *et al.* (2000); Son and Yoon (2001)]. The basis of this measurement is the relationship between the evolution of the drop shape and the interfacial tension. Various phenomenological formulae have been developed by assuming Newtonian rheology in both the drop and the matrix phases, and they typically give similar results [Maffettone and Minale (1998); Jackson and Tucker (2003); Yu and Bousmina (2003)]. Maffettone and Minale's (1998) model, for example, describes the retraction of an ellipsoidal drop by:

$$L^2 - B^2 = (L^2 - B^2)_{t=0} \exp\left[-\frac{\sigma}{\mu_m R_0} f(\beta) t\right], \tag{20}$$

where R_0 is the equilibrium drop radius, μ_m is the matrix viscosity, $f(\beta) = \frac{40(\beta+1)}{(2\beta+3)(19\beta+16)}$ and β is the viscosity ratio between the drop and the matrix. By measuring $L(t)$ and $B(t)$, the half-length and half-width of the drop, the interfacial tension σ can be calculated from curve fitting. Since these models are intended for Newtonian fluids, it is surprising that they give fairly good results for some two-phase systems of flexible polymers [Mo *et al.* (2000)]. On the other hand, if the drop is a thermotropic liquid crystalline polymer, Yu *et al.* (2004a) found that the drop size deviates from the exponential law and the scheme fails.

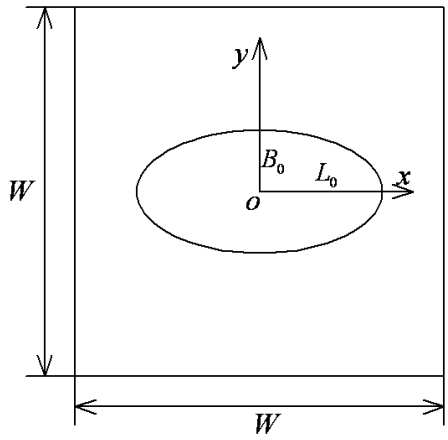

Figure 13: Computational domain for drop retraction.

To explain these experimental findings, we investigate the effects of viscoelasticity and liquid crystallinity, in either the drop or the matrix phase, on drop retraction. One of the two components is Newtonian, while the other is an Oldroyd-B fluid or a regularized Leslie-Ericksen nematic fluid. The calculations are in 2D, but we expect the physical insights gained here to be relevant to the 3D experiments. As in previous theoretical and numerical calculations, we assume the retraction is slow and the fluids are highly viscous so as to render inertia negligible. For simplicity, the two components are assumed to have the same density and same steady-shear viscosity.

The geometry of the problem is shown in Fig. 13. We use periodic boundary condition for both directions and discretize the equations using a Fourier spectral method. Initially, the drop is elliptic with semi-axes L_0 and B_0. We will use the final drop radius $R_0 = \sqrt{L_0 B_0}$ as the characteristic length.

A. Effects of viscoelasticity on drop retraction

Let us first consider the retraction of an elliptic drop from a stationary initial state with zero velocity and zero stress. This is intended to mimic experiments where the elongated drop is produced by melting a filament sandwiched between two sheets of the matrix fluid [Yu *et al.* (2004*a*)]. Depending on how the filament is produced, there may be residual stress frozen inside, but we neglect this possibility. In this subsection the initial geometric

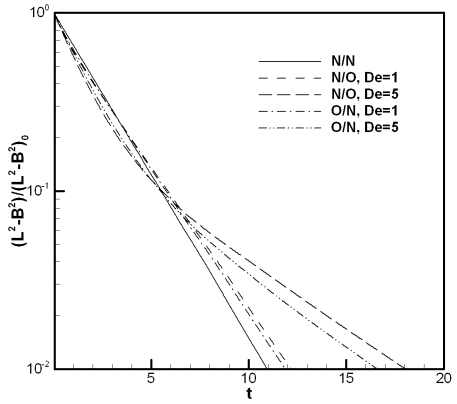

Figure 14: The $L^2 - B^2 \sim t$ curves for drop relaxation from an initially elliptic shape with $D_0 = 0.1$.

parameters are $W = 6$, $L_0 = 1.1055$ and $B_0 = 0.9045$, which correspond to an initial deformation parameter $D_0 = (L_0 - B_0)/(L_0 + B_0) = 0.1$. From the equilibrium drop radius R_0, viscosity μ and interfacial tension σ, we define a characteristic time scale for retraction:

$$t_{ret} = \frac{\mu R_0}{\sigma}. \tag{21}$$

The Deborah number is defined as $De = \lambda_H / t_{ret}$, where λ_H is the relaxation time of the polymer. Note that De differs from its usual definition using a strain rate by a factor that is the capillary number. Two Deborah numbers are simulated: $De = 1$ and 5. The other dimensionless parameters are: $\epsilon = 0.01$, $\lambda = 1.0607 \times 10^{-2}$ (corresponding to $\sigma = 1$). For the Oldroyd-B fluid, the retardation time is one half of the relaxation time.

Figure 14 compares several cases of drop retraction, with a Newtonian drop in an Oldroyd-B matrix (N/O), an Oldroyd-B drop in a Newtonian matrix (O/N), and a Newtonian drop in a Newtonian matrix (N/N) as the baseline. Perhaps surprisingly, the O/N and N/O cases differ very little for the same De. This is because the interfacial tension drives the retraction against resistance from *both* the drop and the matrix, and whether the viscoelasticity occurs in the drop or the matrix, it produces roughly the same amount of resistance. First, the fluids in the drop and in the matrix are subject to roughly equal extension rates, but with opposite signs. At the pointed ends of the drop, for instance, the

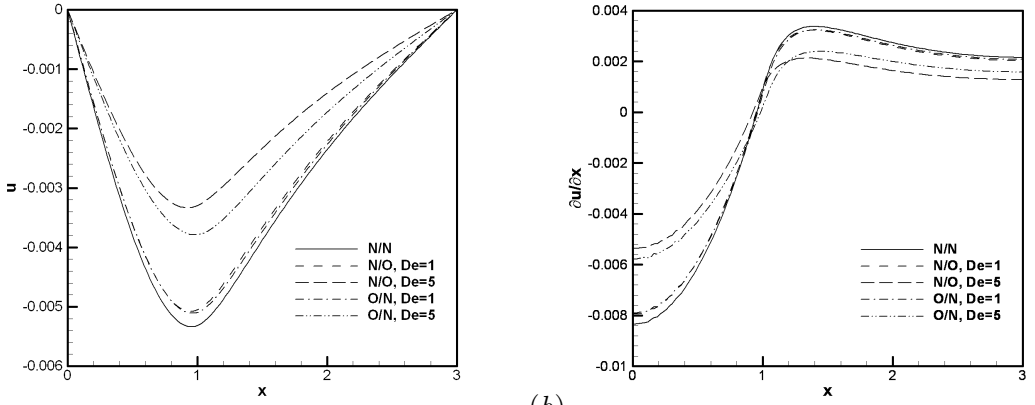

(a) (b)

Figure 15: Local flow profiles across the interface at $t = 5$. (a) $u(x)$; (b) $\partial u/\partial x$. The interface is at $x \approx 1.02$.

interface compresses the drop fluid and stretches the matrix fluid, regardless of their rheology. This can be seen from the velocity profile $u(x)$ in Fig. 15(a); $|u|$ reaches its maximum near the interface (at $x \approx 1.02$) for both N/O and O/N. Furthermore, the velocity gradient $\partial u/\partial x$—or the extension rate—has roughly the same magnitude on both sides of the interface and between N/O and O/N; this is evident from Fig. 15(b). A similar argument can be made at the "waist" of the drop, i.e., the ends of the minor axes.

Second, we may write out the polymer tensile stress for a planar extensional flow $(u, v) = (\dot{\epsilon}x, -\dot{\epsilon}y)$ of an Oldroyd-B fluid [Bird *et al.* (1987)]:

$$\tau_{p,xx} = \frac{2\mu_p\dot{\epsilon}}{1 - 2\lambda_H\dot{\epsilon}}\left\{1 - \exp\left[-\frac{t}{\lambda_H}(1 - 2\lambda_H\dot{\epsilon})\right]\right\}. \tag{22}$$

Given the small value of $\partial u/\partial x$ at the interface, the local Deborah number $|\lambda_H\dot{\epsilon}| \ll 1$. Equation (22) implies that the polymers will produce roughly the same amount of stress if stretched or compressed at the same $|\dot{\epsilon}|$. In other words, between N/O and O/N, the polymer normal stress $\tau_{p,xx}$ has more or less the same magnitude on the polymer side, as does the viscous normal stress on the Newtonian side. Therefore, the total resistance to retraction is roughly the same for the two cases. Hence the proximity of O/N and N/O curves in Fig. 14. This contrasts flow-induced drop deformation [e.g., Mighri *et al.* (1997; 1998)] where the two cases present opposite trends. There, the deformation is driven by a prescribed flow and the interplay between interfacial tension and normal stresses is different.

The second notable feature is the effect of De, which can be explained as in Section III.B. Owing to the finite time needed for stress growth in a viscoelastic fluid, the resistance to retraction is initially weaker than in a Newtonian fluid. Hence, the retraction is faster in the initial stage for N/O and O/N than for N/N. This is reversed later as the viscoelastic stress exceeds the Newtonian stress, and the retraction becomes slower than that for N/N. Not surprisingly, this effect is more pronounced at higher De.

Based on the above discussion, the drop retraction method for measuring interfacial tension is likely to work for viscoelastic fluids if the retraction is slow (due to high viscosity, say), and the Deborah number is small. Otherwise the retraction does not follow an exponential law and the method will fail. Indeed, the experiments of Mo *et al.* (2000) and Son and Yoon (2001) involve retraction times of many hundreds of seconds. Assuming a polymer relaxation time of several seconds, the Deborah number as defined here will be $De \sim 0.01$.

Most previous work on drop retraction deals with a different initial condition: the cessation of a steady shear or elongational flow that has deformed the drop to a steady shape. Compared with the retraction discussed above, a new factor is the initial stress field; the polymer chains are stretched and their relaxation will be coupled with the relaxation of the drop shape. We have simulated drop retraction from initial conditions produced by steady shear at a capillary number of $Ca = 0.1$; Fig. 16 compares the behavior of O/N, N/O and N/N systems. Note that the initial deformation D_0 differs slightly among the 5 runs because of the different viscoelasticity of the components. It is also slightly larger than that in Fig. 14.

Despite the differing D_0, the retraction of an Oldroyd-B drop in a Newtonian matrix (O/N) is very close to that starting with zero initial stress (Fig. 14). In contrast, the retraction of a Newtonian drop in an Oldroyd-B matrix (N/O) is quite different from its counterpart in Fig. 14. The retraction is slower than the N/N case from the very beginning, and the discrepancy grows with time. The effect is also more pronounced for higher De. These observations can be explained by studying the flow field and the polymer stress distribution. During the steady shear prior to retraction, the flow inside the drop is highly rotational in all cases, while outside it is shear or moderately extensional (Fig. 17). Thus,

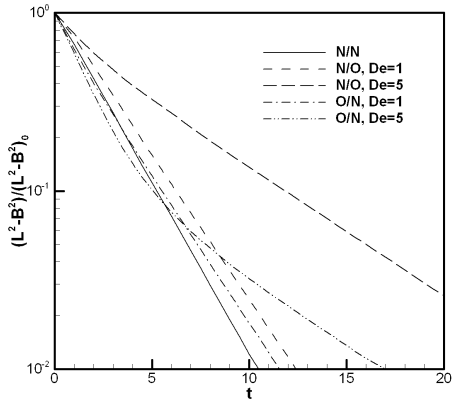

Figure 16: The $L^2 - B^2 \sim t$ curves for drop relaxation from initial conditions produced by steady shear. For the 5 runs, the initial deformation parameters are $D_0 = 0.1078$ (N/N), 0.1065 (N/O, $De = 1$), 0.1035 (N/O, $De = 5$), 0.1072 (O/N, $De = 1$), and 0.1053 (O/N, $De = 5$).

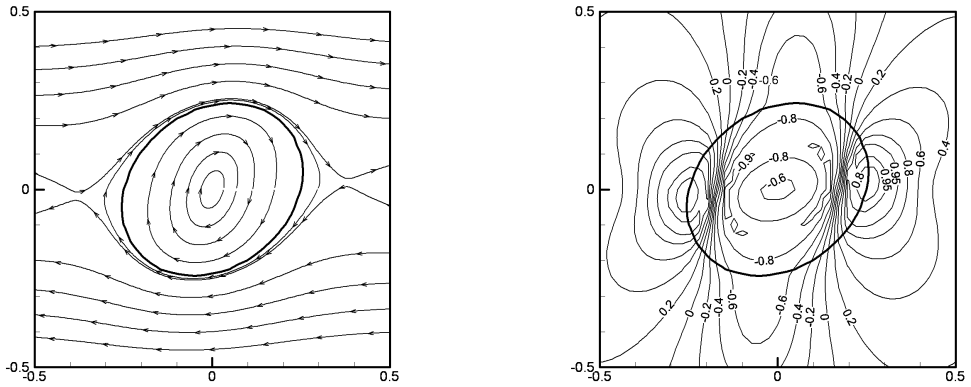

(a) (b)

Figure 17: Streamlines (a) and flow type contours (b) near a drop in steady shear. Both the drop and and the matrix are Newtonian. $Ca = 0.1$. The flow type parameter is defined as $\gamma = \frac{||\boldsymbol{D}||-||\boldsymbol{\Omega}||}{||\boldsymbol{D}||+||\boldsymbol{\Omega}||}$, where $\boldsymbol{D} = \frac{\nabla\boldsymbol{v}+(\nabla\boldsymbol{v})^{\mathrm{T}}}{2}$, $\boldsymbol{\Omega} = \frac{(\nabla\boldsymbol{v})^{\mathrm{T}}-\nabla\boldsymbol{v}}{2}$, and the norm of the matrices is defined by, e.g., $||\boldsymbol{D}|| = \sqrt{\frac{\boldsymbol{D}:\boldsymbol{D}^{\mathrm{T}}}{2}}$.

if the matrix is viscoelastic, a considerable normal stress builds up around the drop. In contrast, if the drop is viscoelastic, there is little polymer stress inside the drop. Figure 18 plots the evolution of the normal stress difference $N_1 = \tau_{nn} - \tau_{tt}$ just outside the end of the drop for N/O and just inside for O/N during retraction, n and t being the local normal and tangential direction. The former is much larger and lasts longer, and explains the

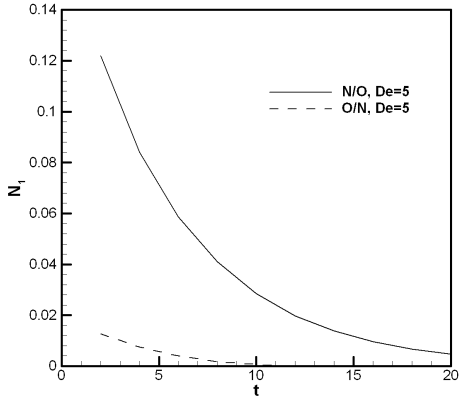

Figure 18: Normal stress difference in the Oldroyd-B fluid near the drop tip. The data are take at the intersection of $\phi = 0.9$ and the major axis of drop. Recall that $\phi = 1$ in the bulk Oldroyd-B fluid.

retarded retraction in the Oldroyd-B matrix. The persistence of polymer stress outside the contracting ends of the drop is partly due to the fact the retraction further stretches the polymer chains or at least postpones their recoiling [Tretheway and Leal (2001)]. This effect is significant since $De = \lambda_H / t_{ret} \geq 1$, with the polymer chain relaxing more slowly than the drop. Also note that for O/N, the small residual viscoelastic stress inside the drop tends to promote drop retraction initially because $N_1 > 0$.

The experiment most relevant to our simulation is that of Tretheway and Leal (2001), who measured the retraction of Newtonian drops suspended in a PIB/PB Boger fluid following planar extensional flow. Although quantitative comparison is precluded by the different flow types and dimensionality, the qualitative trends are the same. In particular, Tretheway and Leal (2001) suggested that the tensile stress induced by the contraction of the drop ends causes the drop retraction to slow down in a viscoelastic matrix. This is essentially borne out by our Fig. 18. In addition, the prediction that persisting polymer stresses in the matrix hinder drop retraction confirms similar predictions by the phenomenological models of Maffettone and Greco (2004) and Yu *et al.* (2004*b*). Hooper *et al.* (2001) computed the retraction of a drop pre-deformed by a uniaxial elongational flow. The cessation of flow, however, is effected by instantaneously freezing the outer boundaries of the computational domain. The induced backflow inside the domain causes the drop to stretch further before retraction.

B. Effects of liquid crystallinity on drop retraction

Liquid crystallinity, be it inside or outside the drop, enters the interfacial dynamics via the anchoring energy f_{anch} [cf. Eqs. (3, 4)]. It is little wonder that drop retraction should be modified qualitatively, and that Newtonian formulae such as Eq. (20) should fail [Yu *et al.* (2004*a*)]. Yue *et al.* (2004) have described one example of the anchoring effects on the retraction of a nematic drop, and Liu *et al.* (2004) have discussed the role of liquid crystallinity in the matrix phase. Our objective here is an in-depth analysis of the physical mechanisms involved in the retraction of a nematic drop in a Newtonian matrix.

We have simulated 3 cases with the drop being Newtonian (baseline case), nematic with *planar* anchoring and nematic with *homeotropic* anchoring. The geometric parameters are $W = 3.9738$, $L_0 = 1.5811$ and $B_0 = 0.6325$. Using the capillary time scale $\mu_m R_0/\sigma$, we make the other parameters dimensionless: $\lambda = 1.342\times10^{-2}$, $\gamma_1 = 4\times10^{-5}$, $\epsilon = 1.265\times10^{-2}$, $\delta = 6.325 \times 10^{-2}$, $K = 6.708 \times 10^{-2}$, $A = 6.708 \times 10^{-3}$ and $\gamma_2 = 10$. Compared with the material constants of common liquid crystals and liquid crystal polymers [Larson (1999)], the anchoring energy A is in the realistic range, while the bulk elastic constant K and director relaxation parameter γ_2 are about an order of magnitude too large. These are used to amplify the novel effects brought on by the liquid crystallinity inside the drop. For planar anchoring, $\boldsymbol{n}$ is initially horizontal everywhere. For homeotropic anchoring, we impose a radial $\boldsymbol{n}$ emanating from the center of the drop. Since the drop is elliptic, the initial $\boldsymbol{n}$ field deviates from the easy direction over much of the interface in both cases.

Figure 19 shows that the nematic drop with homeotropic anchoring retracts faster than the Newtonian drop while the one with planar anchoring is slower than the Newtonian drop. Heuristically, these results can be explained in terms of the anchoring energy f_{anch} [Yue *et al.* (2004)]. Given the initial $\boldsymbol{n}$ fields, the retraction reduces f_{anch} for homeotropic anchoring but increases it for planar anchoring. The final equilibrium shape is circular for homeotropic anchoring, with a hedgehog defect at the center. For planar anchoring, the final shape is prolate. The director field exhibits the well-known *bipolar* configuration with two surface defects at the poles [West (1990); Shen *et al.* (2002)]. If we use smaller and more realistic K values, the bipolar drop will be nearly circular. Using these retraction curves, one may determine an apparent interfacial tension σ_{app} from the Maffettone-Minale formula [Eq. (20)], which is plotted in Fig. 20 for the three cases.

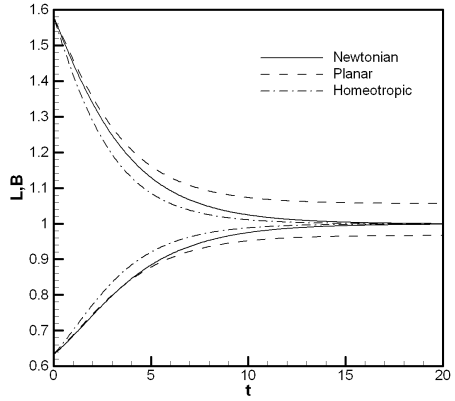

Figure 19: Drop retraction: variation of the major and minor semi-axes for a Newtonian drop and nematic drops with planar and homeotropic anchoring [after Yue *et al.* (2004) ©Cambridge University Press.]

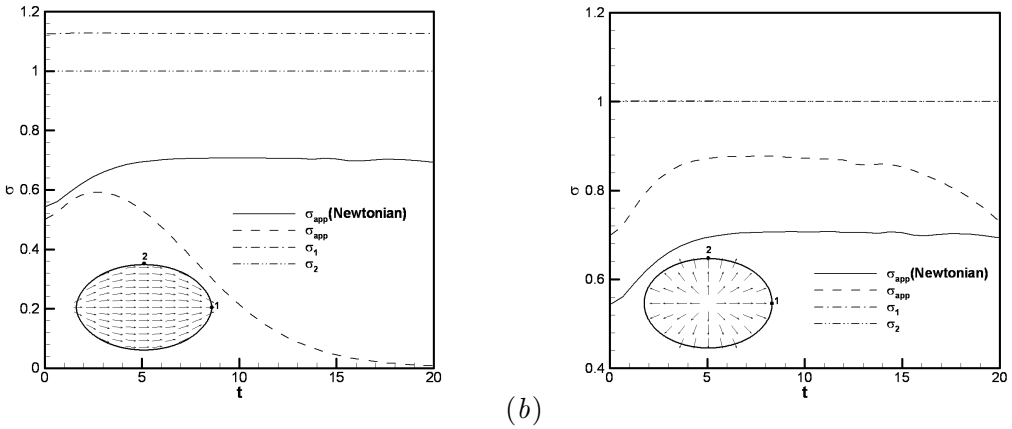

Figure 20: True interfacial tension calculated from the interfacial energy [Eq. (23)] compared with the apparent interfacial tension σ_{app}. (a) Bipolar configuration; (b) homeotropic configuration. The apparent interfacial tension for the Newtonian drop is also shown for comparison.

The remainder of this section is devoted to understanding the correlation between the interfacial energy, the interfacial forces and the drop retraction. First, we note that σ_{app} is not the same as the true dynamic interfacial tension, which varies with time as well as location along the interface. Because our numerical method is based on the free energy, it is very convenient to calculate the dynamic interface tension by equating the interfacial

energy per unit area in the sharp- and diffuse-interface representations:

$$\sigma_{true} = \int (f_{mix} + f_{anch})\, dh, \tag{23}$$

where the integration is performed across the interface. Since f_{anch} may vary along the interface because of different anchoring angles, so may σ_{true}. We plot the true interfacial tension at the tip (Point 1) and waist (Point 2) of the drop in Fig. 20. If there was no anchoring energy, the variation of σ_{true} would be entirely due to the relaxation of the interfacial ϕ profile [Yue *et al.* (2004)]. This effect is very small for the current parameters, and σ_{true} would appear as roughly a constant, which is unity here because of our scaling. For planar anchoring, the directors are almost perpendicular to the interface at Point 1, thus $f_{anch} > 0$ there and the true interfacial tension $\sigma_1 > 1$. At Point 2 the true interfacial tension $\sigma_2 \approx 1$ because the director is always parallel to the interface at that point, which produces zero anchoring energy [cf. Eq. (3)]. By the same token, the homeotropic anchoring is satisfied at both points in Fig. 20(b), and σ_1 and σ_2 both remain roughly constant at unity. The lack of temporal variation of σ_{true} in Fig. 20 is coincidental because our initial conditions are such that f_{anch} barely changes at the two points during the retraction. For points between 1 and 2, σ_{true} should vary in time. The dependence of σ_{true} on the local director anchoring forms an interesting analogy to the Monte Carlo simulations of Li and Denn (2001), although the anchoring energy is postulated here, but manifested by chain interactions between the components in their work. Also note that for the Newtonian drop, $\sigma_{app} < 1$. This is because the Maffettone-Minale formula is intended for three dimensions, and our two-dimensional drop retracts more slowly.

Because the anchoring energy is not constant along the interface, the gradient of the dynamic interfacial tension drives a Marangoni flow. Figure 21(a) shows the velocity field near the nematic drop with planar anchoring toward the end of the retraction. The time scales of our system are such that the slowly relaxing interfacial profile is driving a flow long after the macroscopic retraction has been completed. Note that the flow goes from point 2 to point 1, along the gradient of the interfacial tension. For the radial configuration in Fig. 21(b), the flow is negligible. The Marangoni effect in our diffuse-interface theory is equivalent to that formulated by Rey (2000) in a sharp interface framework.

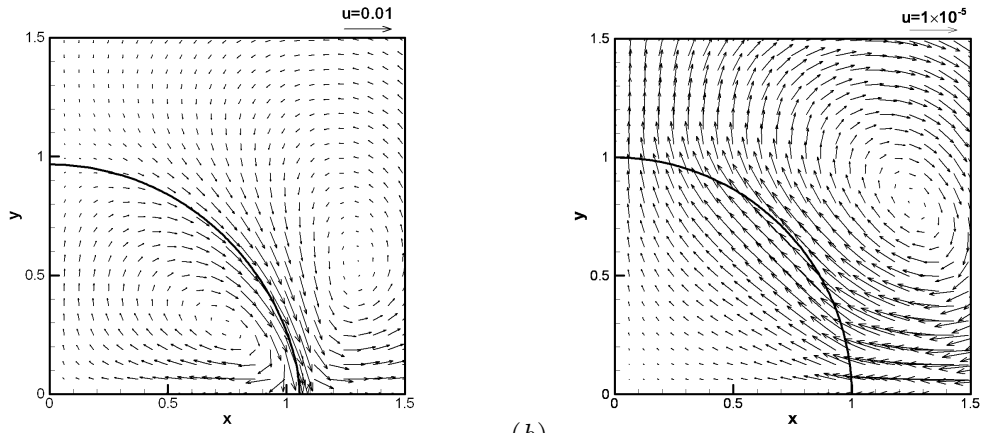

Figure 21: Velocity field at $t = 29.82$ near the nematic drop. (a) Bipolar configuration, where a Maragoni flow prevails. (b) Homeotropic configuration, where the velocity is negligible compared with that in (a).

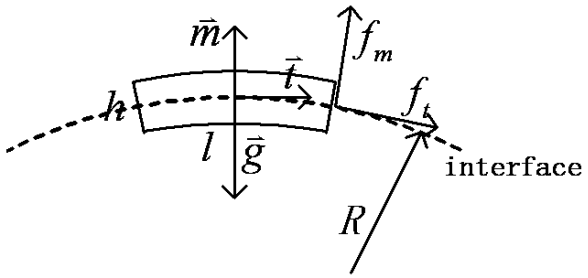

Figure 22: A pillbox control-volume for calculating interfacial forces.

According to the true interfacial tension in Fig. 20, the nematic drop with planar anchoring should retract faster than the Newtonian drop owing to the larger σ_{true}, while that with homeotropic anchoring should retract with roughly the same speed. This expectation is at odds with Fig. 19 because the anchoring energy generates a *normal* surface force in addition to the interfacial tension, which influences the retraction as well. To illustrate this mechanism, we will use the planar anchoring case as an example to analyze the interfacial forces.

Figure 22 shows a pillbox control-volume that covers the interface. Rigorously, the stress tensors due to the mixing energy f_{mix} and the anchoring energy f_{anch} can be written as [cf. Eq. (8)]:

$$\boldsymbol{T}_{mix} = f_{mix}\boldsymbol{I} - \lambda(\nabla\phi \otimes \nabla\phi), \tag{24}$$

$$\boldsymbol{T}_{anch} = f_{anch}\boldsymbol{I} - A(\boldsymbol{n}\cdot\nabla\phi)\boldsymbol{n}\otimes\nabla\phi. \tag{25}$$

Noting that $\nabla\phi$ is parallel to the surface normal $\boldsymbol{m}$ and perpendicular to $\boldsymbol{t}$, we write the tangential and normal tractions on the sides as:

$$f_t = \int (\boldsymbol{t}\cdot\boldsymbol{T}\cdot\boldsymbol{t})\, dh = \int (f_{mix} + f_{anch})\, dh, \tag{26}$$

$$f_m = \int (\boldsymbol{t}\cdot\boldsymbol{T}\cdot\boldsymbol{m})\, dh = -\int A(\boldsymbol{n}\cdot\nabla\phi)(\boldsymbol{t}\cdot\boldsymbol{n})(\nabla\phi\cdot\boldsymbol{m})\, dh, \tag{27}$$

where $\boldsymbol{T} = \boldsymbol{T}_{mix} + \boldsymbol{T}_{anch}$, and the integration is performed across the interface. Now f_t is the conventional interfacial tension as in Eq. (23). But f_m is an additional normal force that stems from the anchoring energy. Although this force does not stretch the interface, it nevertheless affects the retraction of the drop in a way analyzed below.

The total force per unit area due to the interfacial energy is $\boldsymbol{g} = \int(\nabla\cdot\boldsymbol{T})\, dh$, and $g = \boldsymbol{g}\cdot(-\boldsymbol{m})$ is the normal traction pushing inward. In view of the Young-Laplace equation, we may consider gR a local "effective interfacial tension" that determines the retraction of the drop, R being the local radius of curvature. Figure 23(a) plots gR at the tip and waist of the drop with planar anchoring. Our scaling is such that for a Newtonian drop, $\sigma = \boldsymbol{g}\cdot(-\boldsymbol{m})R = 1$. The initial transient ($t \leq 1$) is a numerical artifact due to the relaxation of the initially imposed ϕ profile and the relaxation of director whose initial condition is not the equilibrium state [Yue *et al.* (2004)]. Such relaxations should exist in the true interfacial tension of Fig. 20 as well, but their effects are much weaker there.

For the bipolar configuration, $(gR)_1 < 1 < (gR)_2$. This implies that compared with a Newtonian drop, the normal force pushing inward is stronger at the waist and weaker at the poles. Thus, the nematic drop retracts more slowly than the Newtonian drop as seen in Fig. 19, and the apparent interfacial tension σ_{app}, estimated from the retraction curves, is smaller than that of the Newtonian drop [Fig. 20(a)]. The further divergence of $(gR)_1$ and $(gR)_2$ in time causes σ_{app} to decrease with time. The later fall of σ_{app} toward zero is because the bipolar drop fails to attain a circular shape. In Yu *et al.*'s (2004a) experiment, the retraction indeed produces a σ_{app} that declines in time as in Fig. 20(a). However, the nematic drop retracts to a spherical shape because it contains multiple micro-domains. In this case, the declining σ_{app} is probably a combined effect of f_{anch} and the relaxation of the micro-domains [Yu *et al.* (2004a)].

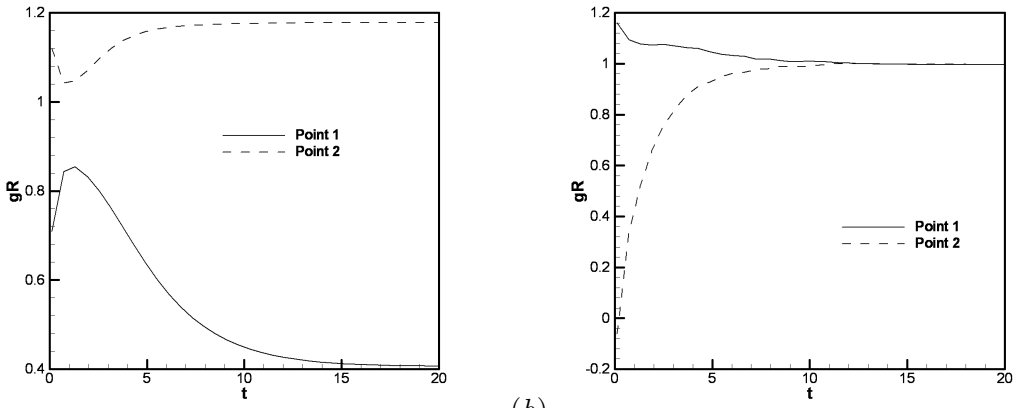

(a) (b)

Figure 23: The effective interfacial tension gR at the waist (Point 1) and pole (Point 2) of the drop, where g is the total normal traction pushing inward, and R is the local radius of curvature calculated by assuming an elliptic drop. (a) Planar anchoring; (b) homeotropic anchoring.

A similar analysis of the surface forces can be carried out for the homeotropically anchored drop [Fig. 23(b)], although the expression for the normal force will differ from Eq. (27). For $t \leq 12$, $(gR)_1 > 1 > (gR)_2$, implying that the anchoring energy will make the retraction go faster than for the Newtonian drop. This explains Fig. 19 as well as the higher σ_{app} in Fig. 20(b). For $t > 13$, $(gR)_2$ exceeds $(gR)_1$ slightly. The retraction of the homeotropic drop is thus hampered toward the end, consistent with the fall of σ_{app} in Fig. 20(b).

To summarize this section, the interfacial anchoring energy f_{anch} plays a fundamental role in the interfacial dynamics of nematic liquids. In particular, it gives rise to a dynamic interfacial tension that may vary along the interface and induce a Marangoni flow. It also induces a normal force on the interface, which influences the drop retraction in addition to the interfacial tension. We confined our discussion here to nematic drops in a Newtonian matrix. The retraction of Newtonian drops in a nematic matrix has been simulated as well and the results have been reported elsewhere [Liu *et al.* (2004)]. Finally, recall that our nematic is represented by a simplified Leslie-Ericksen theory with a single viscosity [cf. Eq. (9)]. Anisotropic viscosities would introduce additional complications in the retraction of the nematic drop.

V. CONCLUDING REMARKS

In this paper, we applied a diffuse-interface formulation to drop coalescence and retraction involving viscoelastic and liquid crystalline fluids, represented by the Oldroyd-B model and a modified Leslie-Ericksen model, respectively. Somewhat coincidentally, in these two processes the non-Newtonian rheology works in much the same way whether it occurs in the drop or in the matrix.

The diffuse interface makes it possible to simulate topological changes such as drop coalescence. The final stage of the coalescence is dominated by short-range molecular forces, and we have shown that the Cahn-Hilliard energy produces such a force comparable with the van der Waals force. Viscoelasticity in either component hastens film drainage and drop coalescence, and the effect can be explained by the relatively slow stress growth in the non-Newtonian component. Drop retraction is generally hindered by viscoelasticity, owing to the persistence of the polymer stresses. For nematic drops, the anchoring energy enters the retraction processes and forms an intrinsic part of the dynamic interfacial tension. In particular, the spatial gradient of the interfacial tension drives a Marangoni flow near the nematic-isotropic interface. Furthermore, the anchoring energy gives rise to an additional normal force on the interface that affects the retraction process in addition to the interfacial tension. As a result, one cannot define an interfacial tension as a material constant between a nematic and an isotropic liquid, much less measure it from the shape evolution during drop retraction. Nevertheless, the retraction of nematic drops reveals the intricate interplay among the mixing, anchoring and bulk energies that is likely to play a role in any physical problem involving nematic-isotropic interfaces.

Acknowledgment: Acknowledgment is made to the Donors of The Petroleum Research Fund, administered by the American Chemical Society, for partial support of this research. J.J.F. was also supported by the NSF (CTS-0229298, CTS-9984402), the NSERC's Canada Research Chair program, and the NNSF of China (No. 20174024). J.S. was supported by the NSF (DMS-0074283, DMS-0311915). C.L. was supported by the NSF (DMS-0405850). We acknowledge discussions with Professor M. M. Denn, Professor W. Yu and Professor C. Zhou.

References

Anderson, D. M., G. B. McFadden, and A. A. Wheeler, "Diffuse-interface methods in fluid mechanics," Ann. Rev. Fluid Mech. **30**, 139–165 (1998).

Bhakta, A., and E. Ruckenstein, "Decay of standing foams: drainage, coalescence and collapse," Adv. Colloid Interface Sci. **70**, 1–124 (1997).

Bird, R. B., R. C. Armstrong, and O. Hassager, *Dynamics of Polymeric Liquids, Vol. 1. Fluid Mechanics* (Wiley, New York 1987).

Bradley, S. G., and C. D. Stow, "Collision between liquid drops," Philos. Trans. R. Soc. Lond. Ser. A **287**, 635–675 (1978).

Cahn, J. W., and J. E. Hilliard, "Free energy of a nonuniform system. III. Nucleation in a two-component incompressible fluid," J. Chem. Phys. **31**, 688–699 (1959).

Chuang, T.-K., and R. W. Flumerfelt, "Dual optical monitoring of axisymmetric thin aqueous film drainage," Rev. Sci. Instrum. **68**, 3839–3842 (1997).

de Gennes, P. G., and J. Prost, *The Physics of Liquid Crystals*, 2nd edition, (Oxford, New York 1993).

Dintenfass, L., "Blood as a near-'ideal' emulsion: a retrospective on the concept of the red cell as a fluid drop, its implications for the structure of the red cell membrane," Biorheology, **27**, 149–161 (1990).

Feng, J., G. Sgalari, and L. G. Leal, "A theory for flowing nematic polymers with orientational distortion," J. Rheol. **44**, 1085–1101 (2000).

Gliklikh, Y., *Global Analysis in Mathematical Physics: Geometric and Stochastic Methods* (Springer-Verlag, New York 1997).

Hooper R.W., V. F. de Almeida, C. W. Macosko, and J. J. Derby, "Transient polymeric drop extension and retraction in uniaxial extensional flows," J. Non-Newtonian Fluid Mech. **98**, 141–168 (2001).

Israelachvili, J. N., *Intermolecular and Surface Forces* (Academic Press, London 1992).

Jackson, N. E., and C. L. Tucker, "A model for large deformation of an ellipsoid droplet with interfacial tension," J. Rheol. **47**, 659–682 (2003).

Jacqmin, D., "Calculation of two-phase Navier-Stokes flows using phase-field modelling," J. Comput. Phys. **155**, 96–127 (1999).

Larson, R. G., *The Structure and Rheology of Complex Fluids* (Oxford University Press, New York 1999).

Li, X., and M. M. Denn, "Influence of bulk nematic orientation on the interface between a liquid crystalline polymer and a flexible polymer," Phys. Rev. Lett. **86**, 656–659 (2001).

Lin, F. H., and C. Liu, "Nonparabolic dissipative systems, modeling the flow of liquid crystals," Comm. Pure Appl. Math. **48**, 501–537 (1995).

Lin, F. H., and C. Liu, "Existence of solutions for the Ericksen-Leslie system," Arch. Rat. Mech. Anal. **154**, 135–156 (2000).

Liu, C., and J. Shen, "A phase field model for the mixture of two incompressible fluids and its approximation by a Fourier-spectral method," Physica D **179**, 211–228 (2003).

Liu, C., J. Shen, J. J. Feng, and P. Yue, "Variational approach in two-phase flows of complex

fluids: transport and induced elastic stress," in *Mathematical Models and Methods in Phase Transitions* ed. by A. Miranville (Nova Publications, 2004).

Liu, C., and N. J. Walkington, "Approximation of liquid crystal flows," SIAM J. Numer. Anal. **37**, 725–741 (2000).

Lowengrub, J., and L. Truskinovsky, "Quasi-incompressible Cahn-Hilliard fluids and topological transitions," Proc. Roy. Soc. Lond. **A 454**, 2617–2654 (1998).

Maffettone, P. L., and F. Greco, "Ellipsoidal drop model for single drop dynamics with non-Newtonian fluids," J. Rheol. **48**, 83–100 (2004).

Maffettone, P. L., and M. Minale, "Equation of change for ellipsoidal drops in viscous flow," J. Non-Newtonian Fluid Mech. **78**, 227–241 (1998).

Mighri, F., A. Ajji, and P. J. Carreau, "Influence of elastic properties on drop deformation in elongational flow," J. Rheol. **41**, 1183–1201 (1997).

Mighri, F., P. J. Carreau, and A. Ajji, "Influence of elastic properties on drop deformation and breakup in shear flow," J. Rheol. **42**, 1477–1490 (1998).

Mo, H., C. Zhou, and W. Yu, "A new method to determine interfacial tension from the retraction of ellipsoidal drops," J. Non-Newtonian Fluid Mech. **91**, 221–232 (2000).

Nemer, M. B., X. Chen, D. H. Papadopoulos, J. Blawzdziewicz, and M. Loewenberg, "Hindered and enhanced coalescence of drops in Stokes flows," Phys. Rev. Lett. **92**, 114501 (2004).

Nobari, M. R., Y.-J. Jan, and G. Tryggvason, "Head-on collision of drops—a numerical investigation," Phys. Fluids **8**, 29–42 (1996).

Peskin, C. S., "A random-walk interpretation of the incompressible Navier-Stokes equations," Comm. Pure Appl. Math. **38**, 845–852 (1985).

Pismen, L. M., "Nonlocal diffuse interface theory of thin films and the moving contact line," Phys. Rev. E **64**, 021603 (2001).

Rey, A. D., "Viscoelastic theory for nematic interfaces," Phys. Rev. E **61** 1540–1549 (2000).

Sethian, J. A., and P. Smereka, "Level set methods for fluid interfaces," Ann. Rev. Fluid Mech. **35**, 341–372 (2003).

Shen, J., "Efficient spectral-Galerkin method. II. Direct solvers of second and fourth order equations by using Chebyshev polynomials," SIAM J. Sci. Comput. **16**, 74–87 (1995).

Shen, Q., C. Liu, and M. C. Calderer, "Axisymmetric configurations of bipolar liquid crystal droplets," Continuum Mech. Thermodyn. **14**, 363–375 (2002).

Son, Y., and J. T. Yoon, "Measurement of interfacial tension by a deformed drop retraction method," Polymer, **42**, 7209–7213 (2001).

Stone, H. A., "Dynamics of drop deformation and breakup in viscous fluids," Ann. Rev. Fluid Mech. **26**, 65–102 (1994).

Tezduyar, T. E., "Computation of moving boundaries and interfaces and stabilization parameters," Int. J. Num. Methods Fluids, **43**, 555–575 (2003).

Tretheway, D. C., and L. G. Leal, "Deformation and relaxation of Newtonian drops in planar extensional flows of a Boger fluid," J. Non-Newtonian Fluid Mech. **99**, 81–108 (2001).

Utracki, L. A., *Polymer Alloys and Blends* (Hanser, 1990).

West, J. L., "Polymer-dispersed liquid crystals," Chapter 32 in *Liquid-Crystalline Polymers*, ACS Symp. Ser. **435**, ed. R. A. Weiss and C. K. Ober (1990).

Yu, W., and M. Bousmina, "Ellipsoidal model for droplet deformation in Newtonian systems," J. Rheol. **47**, 1011–1040 (2003).

Yu, R., W. Yu, C. Zhou, and J. J. Feng, "Dynamic interfacial properties between a flexible isotropic polymer and a TLCP investigated by an ellipsoidal drop retraction method," J. Appl. Polym. Sci. (in press) (2004*a*).

Yu, W., C. Zhou, and M. Bousmina, "Theory of morphology evolution in mixtures of viscoelastic immiscible components," J. Rheol. (submitted) (2004*b*).

Yue, P., J. J. Feng, C. Liu, and J. Shen, "A diffuse-interface method for simulating two-phase flows of complex fluids," J. Fluid Mech. **515**, 293–317 (2004).